Orbit Design for a Satellite Swarm-Based Motion Induced Synthetic Aperture Radiometer (MISAR) in Low-Earth Orbit for Earth Observation Applications

Mark Lützner, Thomas Jagdhuber, *Senior Member, IEEE*, Adriano Camps, *Fellow, IEEE*, Hyuk Park, *Senior Member, IEEE*, Markus Peichl, *Member, IEEE*, Roger Förstner, and Matthias Jirousek

***Abstract*— Soil Moisture and Ocean Salinity mapping by Earth observation satellites has contributed significantly toward a better understanding of the Earth system, such as its hydrosphere or climate. Nevertheless, an increased spatial resolution below 10 km with a radiometric resolution in the range of 2 K–3 K of radiometric data could yield a more complete picture of global hydrological processes and climate change. Operational radiometers, such as SMOS, have already approached prohibitive sizes for spacecraft due to the required large antenna apertures. Therefore, radiometer concepts based on a large number of satellites flying in close proximity (swarms) have been proposed as a possible solution. This article investigates the orbit mechanics of placing a satellite swarm-based motion induced synthetic aperture radiometer (MISAR) in low Earth orbit for Earth observation applications. The aperture synthesis antenna array is formed by a large number of individual antennas on autonomously controlled nanosatellites (deputies) and a correlator antenna in the Y-configuration carried by a chief satellite. The proposed design methodology is based on the optimization of satellite positions within a plane and the subsequent translation of coordinates into initial conditions for general circular orbits (GCOs). This enables a more computationally efficient orbit optimization and ensures the time invariance of the antenna array response. Based on this methodology, simulations have been performed with swarms consisting of up to 96 satellites. Simulations show that the spatial resolution of an aperture synthesis radiometer can be increased to less than 10 km for applications where the requirements on radiometric sensitivity are more relaxed ($\Delta T \sim 3$ K).**

***Index Terms*— Aperture synthesis radiometer, Earth observation, fractionated satellite system, motion induced synthetic aperture radiometer (MISAR), radiometry, satellite formation flight, swarms.**

Manuscript received November 23, 2020; revised April 30, 2021, September 9, 2021, December 27, 2021, and February 4, 2022; accepted February 14, 2022. Date of publication February 18, 2022; date of current version March 31, 2022. *(Corresponding author: Mark Lützner.)*

Mark Lützner, Markus Peichl, and Matthias Jirousek are with the German Aerospace Center, Microwaves and Radar Institute, 82234 Weßling, Germany (e-mail: mark.luetzner@dlr.de).

Thomas Jagdhuber is with the German Aerospace Center, Microwaves and Radar Institute, 82234 Weßling, Germany, and also with the Faculty of Applied Computer Science, Institute of Geography, University of Augsburg, 86159 Augsburg, Germany.

Adriano Camps and Hyuk Park are with the Signal Theory and Communications Department, Universitat Politècnica de Catalunya, 08034 Barcelona, Spain (e-mail: camps@tsc.upc.edu; park.hyuk@tsc.upc.edu).

Roger Förstner is with the Aerospace Department, Universität der Bundeswehr, 85577 Neubiberg, Germany (e-mail: roger.foerstner@unibw.de).

Digital Object Identifier 10.1109/TGRS.2022.3152898

I. Introduction

SOIL Moisture and Ocean Salinity mapping by Earth observation satellites has contributed significantly toward a better understanding of the Earth's climate and hydrosphere. Applications that have directly exploited this data range from weather forecasting to water resource management.

Remote sensing of Soil Moisture and Ocean Salinity is operationally performed by passive microwave instruments at the L-band frequency. Measurements within a 27-MHz frequency band at 1.4 GHz exhibit both high sensitivity to salinity and soil moisture, and low radio frequency interference [1], [2]. Currently, salinity and soil moisture maps are generated by ESA's Soil Moisture Ocean Salinity (SMOS) and NASA's Soil Moisture Active Passive (SMAP) satellites. The two satellites generate data on a global scale with spatial resolutions of 35 to 50 km [3], [4]. Spatial resolutions within the same magnitude are required for the upcoming multifrequency Copernicus imaging microwave radiometer (CIMR) mission of ESA [5]. While L-band radiometer data at these spatial resolutions have proven to be of great value for scientific and societal users [6], an increase in the spatial resolution could further improve existing applications and even enable new ones requiring higher order spatial precision. Hydrological applications ranging from subcatchment-scale water management to field-scale agricultural irrigation would benefit from high-resolution soil moisture maps in the subdecakilometer range [7]. Furthermore, more spatially detailed damage maps after hydrological extremes, such as droughts (e.g., lost crop yield and harvest failure) or floods (e.g., dam bursts and inundated areas), would help to provide a more solid basis for appropriate emergency decision-making [8], [9].

Typically, better geometric resolution in the L-band is achieved by increasing the diameter of the radiometer antenna. However, satellites such as SMOS already have approached prohibitive sizes for spacecraft due to large antenna apertures (∼8 m diameter). In light of progress in satellite formation flying and small satellite technology, a satellite swarm-based aperture synthesis radiometer in low Earth orbit (LEO) might be able to extend or replace radiometers relying on monolithic antenna structures. Such a system would be composed of a large number of formation-flying satellites, each carrying individual antennas as part of an aperture synthesis antenna

array. Swarm-based aperture synthesis radiometers have been investigated in geostationary orbit [10] or in LEO for astronomy purposes [11], [12]. The design of an LEO-based system for Earth observation, however, would face unique challenges:

First, in contrast to interferometric arrays for astronomy applications, a radiometer for Earth observation requires the ability to map extended sources, such as radiation distribution over land surfaces. This entails the need for low antenna side lobes and a high main beam efficiency (MBE) in order to avoid the folding of sidelobe signals into the information retrieval. Second, formation flight in LEO is complicated by strong perturbing forces due the nonspherical shape of the Earth and residual aerodynamic drag. Autonomous high-precision orbit control with propulsion systems is necessary in order to keep satellites on fixed relative orbits. Third, the available observation time for Earth-observing systems is in the order of seconds and not hours, as with systems for astronomical purposes.

The choice of relative orbits for individual satellites impacts the technical feasibility of the swarm radiometer, e.g., fuel consumption, collision risk, and the imaging performance, e.g., spatial resolution or sidelobe level. While the first introduction of such a concept was given by Schwartz [13], a system study considering formation flight and imaging performance aspects has not been carried out to date for LEO.

The contributions of this study are threefold. First, a system concept for a swarm-based aperture synthesis radiometer in LEO for Earth observation applications is introduced. Second, a design method that aims to optimize imaging performance over the selection of relative orbits is presented. This design method is based on a two-step approach. The first step optimizes a 2-D receiver configuration of a fixed number of receivers for spatial frequency coverage. The spatial frequency coverage describes the spatial frequency components of a radiation distribution that is observed by the radiometer during an overflight of a target area. The second step translates the 2-D configuration into orbit parameters for a side-looking radiometer system and determines fuel consumption and imaging performance. Finally, this study offers a performance analysis of an idealized swarm-based aperture synthesis radiometer, considering orbit mechanical constraints.

II. System Concept

The swarm-based aperture synthesis radiometer is composed of the chief satellite and N smaller CubeSat (8U) satellites (deputies) orbiting the chief satellite in close proximity on fixed circular reference orbits (See Fig. 1.). The radiometer antenna is formed by a central monolithic array of the patch antenna and receiver units (ARUs) in the Y-configuration carried by the chief satellite and a single ARU on the free-flying deputies. Both the central and the deputy ARU are oriented in the same side-looking orientation. A foldable array in the Y-configuration was chosen for the central chief array because it enables efficient imaging [14] and can be practically implemented in a spacecraft.

During measurements, all time-synchronized ARUs record electromagnetic emission with the center frequency f_c and bandwidth B. The timestamped digital recordings of the deputy ARU are then transferred to the central satellite via an intersatellite link. Image processing is conducted on the chief satellite using interferometric motion induced synthetic aperture radiometer (MISAR) algorithms [14]. Processed data are then downlinked by a wideband communication system from the chief satellite.

All deputies are equipped with low-impulse three-axis propulsion systems, capable of maintaining their position on the relative reference orbits. In addition, three-axis attitude control systems enable the reorientation of the antenna by conducting slews before and after maneuvers. Relative navigation within the formation is performed on the basis of relative global navigation satellite system (GNSS) measurements of position and velocity. The guidance navigation and control subsystem onboard each deputy regularly determines the satellite state estimates, compares them with the reference state, and determines appropriate thruster responses in a leader–follower approach. Deputies are launched within a canisterized dispenser module on the chief and ejected into their respective relative orbits by impeding small initial velocity increments. The main system will orbit on a circular repeat orbit in at least ∼750-km altitude. This altitude was chosen, as it enables a tradeoff between acceptable atmospheric drag and appealing imaging performance. It also enables a comparison of imaging performance with SMOS. In order to realize a repeat ground track, the system will need to be raised periodically. This necessitates a capability for orbit control of the chief satellite as well.

III. Interferometric Motion Induced Synthetic Aperture Radiometer

Aperture synthesis is a technique using a large number of individual antennas to increase the angular resolution of radiometric systems [15]. It was first developed for astronomical radio telescopes before being adopted for Earth observation, notably by the SMOS satellite. In aperture synthesis, imaging occurs by correlating the signals from individual antennas on a larger array to generate samples of the spatial frequencies of distributed radiation sources. Each baseline formed by an antenna pair on an array of antennas generates a single spatial frequency sample. The imaged spatial source distribution is generated by performing an inverse Fourier transform on the samples of all baselines. A complete system simulator for such systems, the synthetic aperture interferometric radiometer performance simulator (SAIRPS), was developed by Camps *et al.* [16].

A further development of aperture synthesis radiometric systems is the MISAR. It uses the motion of the imaging array to increase coverage of the spatial frequency domain. By introducing time delays in the receiver paths, the image can be focused on a single point on the ground, making it possible to continuously sample an area during the overflight. MISAR is crucial in enabling a swarm-based aperture synthesis radiometer system, as the distance between individual antennas can effectively be increased, without decreasing sampling density.

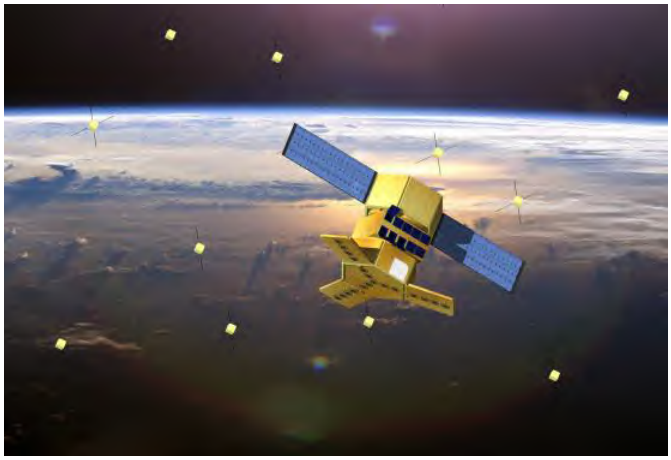

Fig. 1. Artist's visualization of the proposed satellite concept showing the larger chief satellite with the correlator antenna in the Y-configuration and the other CubeSats (deputies) in close proximity.

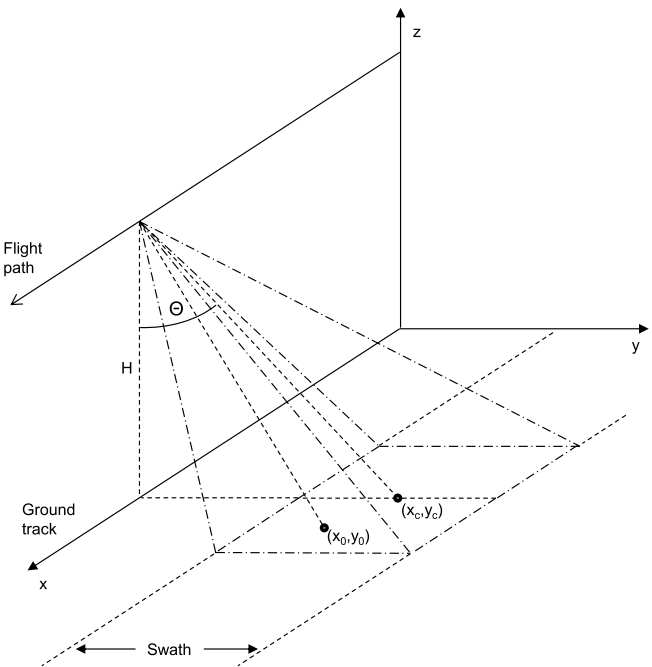

Fig. 2. Observation scenario for a side-looking MISAR system with the system altitude H, an antenna array tilt angle Θ, and a single point source at x_0, y_0.

A. MISAR Observation Model

A simplified observation scenario for a side-looking, Earth-observing MISAR system is depicted in Fig. 2. The system is situated in a quasi-circular orbit, i.e., an orbit with negligible eccentricity, at altitude H continuously scanning a swath along the flight path (x-axis) with an antenna array tilt angle Θ in cross-track direction (y-axis). Assuming a rectangular footprint, each point source within the swath (Width: $2L_y$) is observed from $t = -t_c$ to $t = t_c$ for a duration of $t_{\text{obs}} = 2t_c = 2L_x/v_a$ with a half footprint in flight direction, L_x, and the orbital speed, v_a.

For an MISAR system imaging distributed sources, the estimated brightness temperature $\hat{T}(x_0, y_o)$ at a point x_0, y_0 within the swath is given by Park and Yong-Hoon [17] as

$$\hat{T}(x_0, y_o) = \int_{\bar{y}-L_y}^{\bar{y}+L_y} \int_{-v_a t_c - L_x}^{v_a t_c + L_x} T(x, y) \cdot \text{AFeq}(x_0 - x, y_0 - y) dx dy \tag{1}$$

where y_c is the center point of the footprint across-track and AFeq is the equivalent array function. The equivalent array function AFeq in (1) describes the response of an aggregated array to a single point source at x_0, y_0 within a footprint area. It can, thus, be used to gauge the effectiveness of the array configuration in sampling the spatial frequency domain and is also referred to as the point spread function (PSF). The equivalent array function AFeq is defined as

$$\text{AFeq}(x_0 - x, y_0 - y) = \frac{\sum_j \bar{W}_j \text{AF}_j(x_0 - x, y_0 - y)}{\sum_j \bar{W}_j} \tag{2}$$

which is the weighted sum of the baseline array functions AF_j from each baseline j. The baseline array function represents the point source response of a single baseline. The weights $\bar{W}_j$ denote the average weights of the array functions for each baseline. Equation (2) is normed by a sum of the weights $\sum_j \bar{W}_j$ to correct for the weighting of the individual baselines. This factor was added to the definition given by Park and Yong-Hoon [17]. The array function for each baseline can be calculated as

$$\text{AF}_j(x_0 - x, y_0 - y) = \frac{C}{2t_c} \int_{-tc}^{t_c} F_n(x, y) \cdot e^{-\pi B^2 \Delta\tau^2} e^{-j2\pi f_0 \Delta\tau} dt \tag{3}$$

where f_0 is the center operating frequency of the system and $C = kB\varphi$, with k denoting Boltzmann's constant, B the receiver bandwidth, φ the beam filling factor, and $F_n(x, y, t) = \exp - (y - y_c)^2/2L_y^2 \cdot \exp - (x - v_a t)^2/2L_x^2$ the normalized antenna voltage pattern. The MISAR delay is given as $\Delta\tau$, which denotes the time delay of the signal between the focused pixel x_0, y_0 and other pixels at x, y. The expression $\exp\{-\pi B^2 \Delta\tau^2\}$ in (3) is the fringe-washing function that accounts for spatial decorrelation effects.

Within the radiometric community, the visibility samples are commonly charted on a spatial frequency plane (often referred to as the (u, v) plane) [17]. The (u, v) plane represents the 2-D frequency spectrum in space, where "u" denotes the spatial frequencies in the in-track and "v" denotes the spatial frequencies in the across-track direction normalized by the wavelength λ of the center measurement frequency. The visibility samples are represented on the (u, v) plane by the baseline projections onto a plane perpendicular to the observation direction.

IV. High-Precision Autonomous Formation Flight

A. Reference Orbits

In the satellite swarm-based MISAR system, the receiver configuration is linked intrinsically to the relative orbits of the deputy satellites around the chief satellite. The choice of satellite orbits for a swarm-based aperture synthesis radiometer

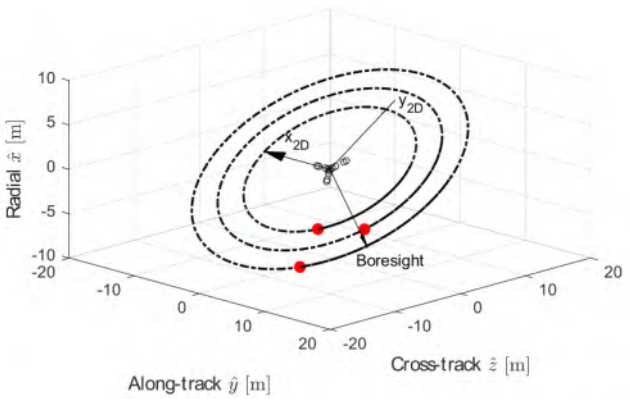

Fig. 3. Example of three deputy satellites (red filled circles) flying on GCO around the chief satellite (black circles) in the Hill frame. The Cartesian coordinate system is spanned by the axes X_{2D}, Y_{2D} which lies within the shared GCO orbit plane. This system is called the optimization frame in Section V. The boresight vector specifies the direction of observation and is perpendicular to the optimization frame.

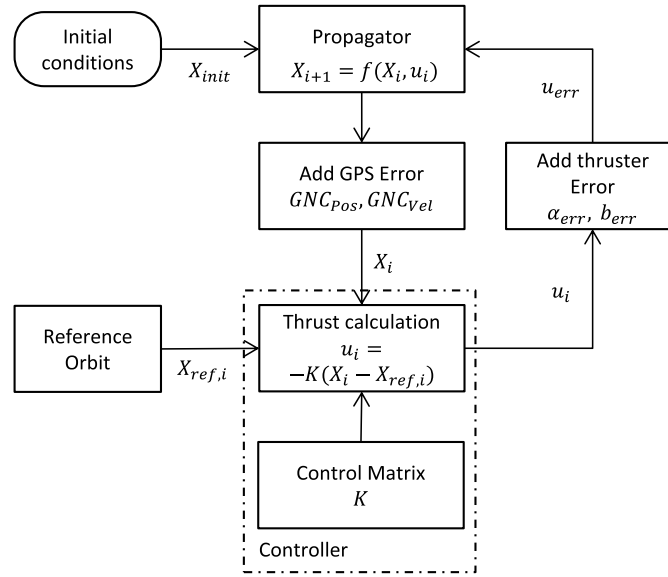

Fig. 4. Block diagram for the DLQR-controller for orbit maintenance of deputy satellites.

must take into account the imaging performance requirements and the system feasibility requirements, i.e., collision avoidance and fuel consumption. From a radiometry perspective, receivers are most effectively placed within a plane facing the center point of the across-track footprint at y_c [18]. On the other hand, the deputy relative orbits should not intersect to avoid collisions. These two requirements strongly favor the satellite arrangement on relative general circular orbits (GCOs). An idealized, keplerian formulation of the GCO can be given in the Hill frame by

$$X_{\text{ref}} = \begin{bmatrix} \hat{x} \\ \hat{y} \\ \hat{z} \\ \dot{\hat{x}} \\ \dot{\hat{y}} \\ \dot{\hat{z}} \end{bmatrix} = \begin{bmatrix} 0.5 \cdot d \cdot \cos(n \cdot t_{\text{GCO}} + \alpha_0) \\ -d \cdot \sin(n \cdot t_{\text{GCO}} + \alpha_0) \\ 0.5 \cdot \sqrt{3} \cdot d \cdot \cos(n \cdot t_{\text{GCO}} + \alpha_0) \\ -0.5 \cdot d \cdot n \cdot \sin(n \cdot t_{\text{GCO}} + \alpha_0) \\ -d \cdot n \cdot \cos(n \cdot t_{\text{GCO}} + \alpha_0) \\ -0.5 \cdot \sqrt{3} \cdot d \cdot n \cdot \sin(n \cdot t_{\text{GCO}} + \alpha_0) \end{bmatrix} \quad (4)$$

with d being the distance to the satellite center, n the orbital rate, α_0 the argument of latitude, and t_{GCO} the time [19]. As an example, Fig. 3 depicts three satellites on GCO around the chief. The relative orbit plane is tilted 30° in the cross-track direction, and the orbits will appear circular with respect to the observation direction.

By varying the distance d and the angle α_0 of individual satellites, the recreation of any 2-D receiver pattern can be realized within the relative orbit plane. The deputies will then rotate around the chief satellite over the course of one orbit while maintaining their distances amongst each other. This satellite configuration has two advantages. First, the circular trajectories of the deputies make it easier to design an array with a circular symmetric array response function. This is because the intersatellite distances stay roughly constant when deputies are placed on circular trajectories. A circular symmetric array response results in similar system responses over all latitudes, as the receiver configuration effectively rotates around the system array boresight once per orbit, with minor changes of the response function. Thus, the optimization of the deputy configuration can focus on optimizing the configuration at a single point in time.

Second, as it will be shown in Section V, placing the satellite on a plane enables the optimization of the receiver, i.e., deputy configuration, within a 2-D plane, with two Cartesian coordinates per deputy instead of three for the 3-D space. This greatly simplifies the numerical optimization of the deputy orbital configuration and, thus, the definition of the individual orbit parameters.

Equation (4) enables the formulation of initial conditions for each deputy satellite that is placed on a GCO. Due to orbital perturbations, most notably from Earth oblateness and aerodynamic drag, a satellite will drift from the idealized reference orbit. Close proximity operations, as required for a dense swarm-based aperture synthesis antenna array, necessitate fully autonomous control of each deputy.

B. Deputy Autonomous Control

In order to investigate the orbit mechanical feasibility of the system concept, it is important to understand the relationship between the choice of relative orbit, position control accuracy, and fuel consumption of the deputies. Ultimately, this enables a realistic estimation of system lifetime and the permissible minimum satellite separation within the aperture synthesis antenna array.

The discrete-time linear quadratic regulator (DLQR) control method is widely used for satellite impulsive formation maintenance [19]. It can be easily implemented on small satellite hardware as it is computationally efficient. A block diagram of the DLQR controller is depicted in Fig. 4. For this study, the DLQR method was implemented as follows. First, deputy states are propagated from initial conditions determined by (4) using the nonlinear relative orbit model of Xu and Wang [20]. This model considers J_2-perturbations as a result of Earth's oblateness. An extension to the model is

made for differential aerodynamic drag affecting the deputies and the chief [21]. The differential aerodynamic drag is a result of different ballistic coefficients and different ratios of spacecraft cross-sectional area and mass. Second, guidance, navigation, and control (GNC) measurement errors in position $\mathrm{GNC_{Pos}}$ and velocity $\mathrm{GNC_{Vel}}$ are subsequently added to the propagated state. In the implemented system, relative position and velocity estimates are acquired through carrier-phase differential GNSS (DGNSS) measurements and orbit propagation data. An extended Kalman filter (EKF) [19] then processes the DGNSS measurements and the orbital data to derive accurate estimations of the satellite state. For simplicity, the simulations conducted within this study assume a Gaussian behavior of the EKF output, with variances in position and velocity taken directly from the navigation solution of the PRISMA mission [22]. GPS blackouts are not considered, and thus, it is assumed that the statistical nature of the GNC error is time-independent. The corrective impulsive control thrust u_i is calculated by

$$u_i = -K\left(X_i - X_{\mathrm{ref},i}\right) \tag{5}$$

with the tracking error $(X_i - X_{\mathrm{ref},i})$, the reference state $X_{\mathrm{ref},i}$, and the current state X_i at timestep i and the control matrix K. The reference state $X_{\mathrm{ref},i}$ is determined from the Keplerian formulation of the GCO, as stated in (4). The discrete control matrix K represents the gain of the feedback controller. The discrete control matrix K is determined by solving the discrete algebraic Riccati equation (DARE) using the state-space representation of the Keplerian dynamics and weighting matrices. The weighting matrices are adopted from the ones used in the CubeSat formation flying CanX-45 mission [23]. The CanX-45 mission was chosen as a reference since its high-precision formation flying demonstration with 8U CubeSats represents a similar scenario to the one proposed within the context of this study. The calculation of the control matrix is described in detail in Appendix I [23]. Finally, a Gaussian thrust magnitude error u_{err} and a Gaussian thrust vector error α_{err} are added to u_i before the state X_{i+1} is propagated for the next time step. The described algorithm is run every control period T_{pwm}, which is the time between two timesteps for regular formation-keeping maneuvers (FKMs). Control thrusts are implemented in a pulsewidth modulation (PWM) method, where the duration of thrust pulses in a control period determines the thrust magnitude.

This control model was chosen because it has been validated by the CanX-45 mission, and it is simple to adjust the control accuracy with the discrete control period T_{pwm}. In general, a shorter control period will ensure a lower deviation of the deputy orbit from the reference GCO. The drawback of a shorter control period is the reduced time for the primary science operation, as imaging can only be conducted when no maneuvers are being performed. This is because the ARU need to be oriented toward x_c, y_c during measurement.

C. Collision Avoidance

Despite regular FKM, there is still the risk of collision within a large densely packed aggregated array of satellites. To mitigate this risk, additional maneuvers will need to be performed in case the distance between deputies falls below a safety distance R_{Coll}. The collision avoidance maneuvers (CAMs) are essentially conducted in the same fashion as the FKM, only that they are triggered immediately upon violation of the safety distance. In order to quantify the required frequency of these maneuvers, the method of Patera [24] is applied. The position uncertainty $\tilde{X}_m$ of a deputy satellite m in the Hill frame can be described by a Gaussian distribution $\tilde{X}_m = N(0, P_m)$. The covariance matrix P_m can be approximated by the mean 3-D root mean square (rms) accuracy σ_m of position control. P_m is assumed to be time-invariant and isotropic. The covariance of the distance δX_k between two deputies, i.e., pair k, can then be calculated as the sum of the position control accuracy covariance of both satellites $\sigma_k = \sigma_m + \sigma_{m+1}$. With the combined covariance σ_k, the probability density function of δX_k is given as

$$\mathrm{pdf}(\delta X_k) = 1/\left(\sqrt[3]{2\pi}\,\sigma_k^3\right) \cdot e^{\left(-\frac{1}{2}\frac{\delta X_k{}^2}{\sigma_k^2}\right)}. \tag{6}$$

The probability of violation of the safety distance, $P_{\mathrm{Coll},k}$, between pair k during one orbit can be calculated by integrating (6) over the volume that is carved out by a circular region of radius R_{Coll} along the relative trajectory of one deputy around the other. Since each deputy pair circumvents each other at a nominal distance of $\delta\bar{X}_k$ on a GCO, the integration region resembles a torus with a ring radius of R_{Coll} and a major radius of $\delta\bar{X}_k$. $P_{\mathrm{Coll},k}$ is given as

$$P_{\mathrm{Coll},k} = \frac{1}{\sigma_k}\sqrt{\frac{2}{\pi}}e^{\left(-\frac{\left(\delta\bar{X}_k{}^2+R_{\mathrm{Coll}}^2\right)}{2\sigma_k^2}\right)} \cdot \int_{-R_{\mathrm{Coll}}}^{R_{\mathrm{Coll}}} \sinh\left(\frac{\delta\bar{X}_k\sqrt{R_{\mathrm{Coll}}^2 - z^2}}{\sigma_k^2}\right) dz. \tag{7}$$

The total probability of violating any safety distance per orbit for a single deputy is then given as the sum of the probabilities of violating the distance with any other deputy

$$P_{\mathrm{Coll},m} = \sum_{1}^{N_k} P_{\mathrm{Coll},k}$$

with N_k being the number of possible collision partners, i.e., the other deputies. The probability of violation of the safety distance $P_{\mathrm{Coll},m}$ for a satellite during one orbit period can then be used to estimate the frequency of required additional CAM.

V. Array Optimization

The placement of satellites on GCO allows the creation of an aggregated rotating, side-looking planar receiver array. Within the planar relative orbit plane, deemed in the optimization frame, the initial relative position of a deputy m may be described by two Cartesian coordinates $X_{2D,m} = [x_{2D,m}, y_{2D,m}]^T$. This coordinate system lies within the GCO plane with the chief satellite as its origin. The x-axis is oriented along the flight direction, and the y-axis completes a right-hand system with the boresight vector (see Fig. 3). The positions of the deputies within this plane can be optimized for the imaging performance of the swarm-based radiometer.

Often applied metrics for imaging performance of an aperture synthesis antenna array are spatial resolution, the magnitude of the sidelobes, and the MBE, i.e., the ratio of energy within the main beam and the sidelobes [15]. Optimizing directly for these quantities would require the calculation of the PSF for each iteration within a numerical optimization algorithm. Since this involves significant computational effort, most methods [25] for the optimization of receiver configurations seek to achieve a desired (u, v) plane coverage.

A study with pseudorandom arrays conducted by Woody [26] for radio telescopes revealed that, ideally, a dense homogenous Gaussian distribution of samples in radial direction yields the lowest sidelobes on interferometric arrays. Any optimization must, thus, recreate a sample distribution in the (u, v) plane that is homogenous in azimuth and of Gaussian form in the radial direction from the origin. Woody [26] showed that a denser sample distribution with a given number of receivers will lower side lobes but will decrease the spatial resolution. The Gaussian distribution must, thus, be iteratively found by setting a target for the sidelobe levels. The following method numerically optimizes the initial positions $X_{2D,m}$ of N receivers in the optimization frame (see Fig. 3).

A. Generation of Spatial Frequency Coverage

For reasons of computational efficiency, the optimization algorithm makes two simplifications: First, the relative motion of satellites is neglected during the flyover. This is tolerable since the evolution of sampled spatial frequencies is mostly dominated by the aspect angle change due to the passing of the satellite system over a target area. Second, the satellite system is moving over a plane surface (see Fig. 2).

Each spatial frequency sampled by the baseline j at the discrete time step $t_i \in \{-t_c, -t_c + \Delta t, \ldots, t_c$ can be expressed in a vector notation $U_{j,i} = [u_{j,i}, v_{j,i}]^T$ in the (u, v) plane. The spatial frequency vector can be determined from the initial baseline vector $\delta X_{2D,j} = X_{2D,m+1} - X_{2D,m}$ and the satellite motion as follows:

$$\begin{aligned} U_{j,i} &= \begin{bmatrix} u_{j,i} \\ v_{j,i} \end{bmatrix} \\ &= A \cdot \begin{bmatrix} y_c^2 + H^2 & y_c \cdot x_s(t_i) & -H \cdot x_s(t_i) \\ y_c \cdot x_s(t_i) & x_s(t_i)^2 + H^2 & y_c \cdot H_0 \end{bmatrix} \\ &\quad \cdot R_{x,30} \cdot \delta X_{2D,j} \end{aligned} \tag{8}$$

with

$$A = \frac{\sqrt{y_c^2 + H^2}}{\lambda \cdot \left(x_s(t_i)^2 + y_c^2 + H^2\right)^{\frac{3}{2}}} \tag{9}$$

and

$$R_{x,30} = \begin{pmatrix} 1 & 0 & 0 \\ 0 & 0.5\sqrt{3} & -0.5 \\ 0 & 0.5 & 0.5\sqrt{3} \end{pmatrix}$$

where $x_s(t_i) = v_a t_i$ is the reference position of the chief satellite during the flyover of the target [17]. The matrix $\mathrm{Rot}_{x,30}$ is required in order to consider the 30° tilt of the GCO (see Fig. 3). The aggregated sampling of the (u, v) plane is simply the sum of all sampled frequencies $U_{j,i}$.

B. Optimization Problem Formulation

In mathematical optimization, an objective function is minimized by the systematic selection of appropriate values from an allowed set as input values and the calculation of the function value. The numerical objective function f must, thus, be defined to ensure a dense Gaussian sampling of the spatial frequency domain in the radial direction and a uniform sampling in the azimuthal direction.

Each spatial frequency vector $U_{j,i}$ on the (u, v) plane is weighted according to the distance from the origin, $|U_{j,i}|$ and the number of sample points $N_{\mathrm{cell},j,i}$ within a grid cell. The objective function is similar to the one used in the "Sieving algorithm" by Su [27]. It is defined as

$$f(x) = \sum_{j}^{N_R} \sum_{i}^{N_T} N_{\mathrm{cell},j,i}^{-1} \cdot e^{-\frac{1}{2} \cdot \left(\frac{|U_{j,i}|}{\sigma_{\mathrm{Gauss}}}\right)^2} \tag{10}$$

with σ_{Gauss} being a parameter with which the density of the samples can be controlled, N_R the number of samples, and N_T the number of time steps. N_R also includes the complex conjugate samples and is, thus, double the number of physical baselines. This definition of the objective function ensures that samples that are farther away from the origin, and those in dense regions of the (u, v) plane are downweighted. For the simulations in Section V, the resolution of the Cartesian grid on the (u, v) plane was set to a single wavelength.

The optimization must also take into account a minimum distance between the deputies $D_{\min,D}$ and a minimum distance to the center satellite $D_{\min,C}$. With these conditions, the optimization problem can be defined as

$$\begin{aligned} &\min_x \ f(x) \\ &\text{s.t. } D_{\min,D} \le |\delta X_{2D,j}|, \quad j = 1, \ldots, N_R \\ &\qquad D_{\min,C} \le |X_{2D,m}|, \quad m = 1, \ldots, N. \end{aligned} \tag{11}$$

C. Solution of Optimization Problem

The optimization problem can be solved using standard algorithms that are capable of finding global solutions for nonsmooth functions subject to nonlinear boundary conditions. Within the course of this study, both the pattern search and the genetic algorithm consistently converged toward similar solutions. The simulations in Section VIII were conducted using the well-known augmented Lagrangian pattern search (ALPS) algorithm [28]. The ALPS algorithm for nonlinearly constrained optimization is not reliant on gradients or higher derivatives but is based on calculating solutions for a constructed mesh. Initial conditions are generated by randomly selecting receiver coordinates. The stopping criteria were set to a mesh tolerance of $1E$-6 or a maximum computation time of 14 h per configuration.

D. Translation of Optimization Frame Coordinates Into GCO Initial Conditions

The translation of the deputy positions from the optimization coordinate system to initial conditions within the Hill

frame is performed by calculating the distance and angle

$$d_m = |X_{2D,m}|\alpha_{0,m} = \arctan2\left(\frac{y_{2D,m}}{x_{2D,m}}\right) \tag{12}$$

for each deputy. These parameters are then inserted into (4) to obtain the initial Cartesian conditions for the GCO. These initial conditions are then used to define the reference orbit for the autonomous control of the deputy satellites.

VI. Baseline Weighting

Due to the constraints, the chief array, and the limited number of deputies, the optimization process will yield an irregular sampling of the (u, v) plane. There will inevitably be local areas within the (u, v) plane that will be sampled denser than others. Without corrective weighting, this would ultimately result in a distortion of the recovered brightness temperature image, as calculated by (1). In order to correct for inhomogeneities, a gridless weighting scheme is applied to the spatial frequency samples. This method has been applied in very long baseline interferometry (VLBI) [29]. It weights each spatial frequency sample according to the number of spatial frequency samples in its proximity on the (u, v) plane. The weights $D_{\text{gridless},j,i}$ are defined as

$$D_{\text{gridless},j,i} = \frac{1}{N_{\text{Weight},j,i}} \tag{13}$$

with $N_{\text{Weight},j,i}$ denoting the number of samples within the radius r_{Weight} from the sample of baseline j and time step i in the (u, v) plane. For the simulations within this study, a value of $r_{\text{Weight}} = 3\lambda$ has shown to yield the best results. The value for r_{Weight} is an empirically determined value that captures the differences in sample density most effectively. In addition to the gridless weighting scheme, a Blackmann tapering function [15] is applied to each sample

$$D_{\text{Blackmann},j,i} = 0.42 + 0.5 \cdot \cos\left(\pi \cdot \frac{|U_{j,i}|}{\rho_{\max}}\right) + 0.08 \cdot \cos\left(2\pi \cdot \frac{|U_{j,i}|}{\rho_{\max}}\right). \tag{14}$$

The tapering function weighs each sample according to its distance to the origin $|U_{j,i}|$, which reduces the sidelobes in the PSF of the array. The value $\rho_{\max}$ is chosen to be the radius at which a uniform Gaussian distribution with the same standard deviation as the actual sample distribution takes a value of 20%.

The total composite weights are, thus, given as

$$W_{j,i} = D_{\text{gridless},j,i} \cdot D_{\text{Blackmann},j,i}. \tag{15}$$

In order to accommodate the time-variant baseline weighting in the definition of the brightness temperature, (2) is extended to

$$\text{AFeq}(x_0 - x, y_0 - y) = \frac{\sum_j \sum_i W_{j,i}\text{AF}_{j,i}(x_0 - x, y_0 - y)}{\sum_j \sum_i W_{j,i}} \tag{16}$$

TABLE I
Payload Properties

Antenna Parameters	Values	Units
Number of antennas per arm	$N_{arm} = 13$	
Centre frequency	$f_c = 1.4$	GHz
Receiver noise bandwidth	$B = 7$	MHz
System Temperature	$T_{sys} = 280$	K
Half-power beamwidth in elevation	$BW_{El} = 62$	deg
Half-power beamwidth in azimuth	$BW_{Az} = 62$	deg
Chief antenna tilt angle	$\Theta = 30$	deg

with

$$\text{AF}_{j,i}(x_0 - x, y_0 - y) = \frac{C}{2t_c} \cdot \int_{t_i+\Delta t/2}^{t_i-\Delta t/2} F_n(x, y) \cdot e^{-\pi B^2 \Delta\tau^2} e^{-j2\pi f_0 \Delta\tau} dt. \tag{17}$$

This assumes a time step of $\Delta t \ll 2t_c$ to still ensure continuous sampling.

VII. Radiometric Sensitivity

The radiometric sensitivity of the interferometric system can be calculated by

$$\Delta T = \frac{\Omega_{\text{ant}}}{\Omega_{\text{pix}}} \cdot \frac{T_{\text{sys}}}{\sqrt[4]{2} \cdot \sqrt{B\tau_{\text{eff}}}} \frac{\sqrt{\sum_j \bar{W}_j^2}}{\sum_j \bar{W}_j} \tag{18}$$

with T_{sys} being the system noise temperature, Ω_{ant} the solid angles of an individual antenna, Ω_{pix} the solid angle of a resolved pixel, i.e., the array resolution, and τ_{eff} the effective integration time [30]. The average weights $\bar{W}_j$ are simply calculated by averaging the weights $W_{j,i}$ of a baseline j over all timesteps i. Equation (18) assumes a single sideband receiver and a Gaussian predetection filter. The effective integration time τ_{eff} can be calculated by $\tau_{\text{eff}} = (t_{\text{obs}}/2 \cdot 1.14)$. This assumes dual-polarization imaging and the usage of 2×2 bit digital correlators and a sampling frequency of four times the measurement bandwidth [31]. It is assumed that the entire overflight time is used for observation [15]. From (18), it can be seen that the introduction of weighting will always lead to a lower radiometric sensitivity. Weighting, however, is necessary for the homogenization of the sampling plane and, thus, a prerequisite for achieving low sidelobes. A derivation of (18) is given in the Appendixes.

VIII. Numerical Simulations

Numerical simulations are conducted on a mission scenario in order to demonstrate the design methodology described above. Simulations are conducted in MATLAB 2019b with system parameters in Tables I–III.

The orbit parameters in Table III are the semimajor axis a, the inclination i, the eccentricity e, the Right Ascension of the Ascending Node (RAAN) Ω, the argument of perigee ω, and the mean anomaly M.

The individual receivers on the Y-antenna of the chief are placed at a distance that is equal to 0.89 wavelengths. There

TABLE II
SPACECRAFT PROPERTIES

Antenna Parameters	Values	Units
Nominal thrust (Deputy)	$u_{Nominal} = 25$	mN
Minimum Impulse Bit (Deputy)	$u_{min} = 0.2$	mNs
Specific Impulse (Deputy)	$I_{sp} = 40$	s
Propellant Mass (Deputy)	$m_{prop} = 300$	g
GNC position knowledge 1σ (Deputy)	$GNSS_{Pos} = 5$	cm
GNC velocity knowledge 1σ (Deputy)	$GNSS_{Vel} = 0.21$	mm/s
Thrust vector error (Deputy)	$\alpha_{err} = 2$	deg
Thrust magnitude error (Deputy)	$u_{err} = 5$	%
Control period (Deputy)	$T_{pwm} = 900$	s
Chief Spacecraft mass	$m_{Chief} = 1163$	kg
Chief Spacecraft aerodynamic area	$A_{Chief} = 9.05$	m^2
Chief Spacecraft ballistic coefficient	$B_{C,Chief} = 2.4$	kg/m^2
Deputy Spacecraft mass	$m_{Deputy} = 6.85$	kg
Deputy Spacecraft aerodynamic area	$A_{Deputy} = 0.12$	m^2
Deputy Spacecraft ballistic coefficient	$B_{C,Deputy} = 2.2$	kg/m^2

TABLE III
KEPLERIAN ORBITAL ELEMENTS OF THE REFERENCE SATELLITE

a [km]	i [°]	e	Ω [°]	ω [°]	M
7121.76	97.53	0	54.95	0	0

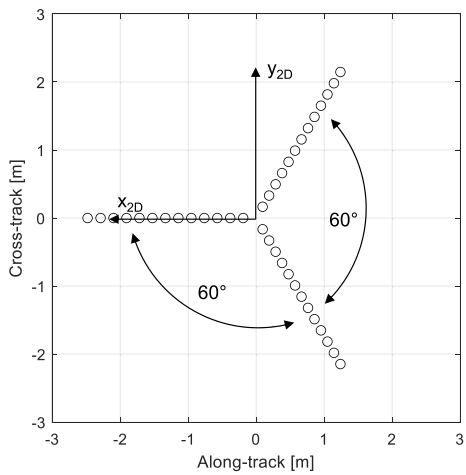

Fig. 5. Central array configuration on the chief satellite with a total of 13 ARU on each beam. The axes X_{2D}, Y_{2D} form the optimization frame. (see Fig. 3).

are a total of 13 ARU placed on each beam. This number of ARU was chosen because a preliminary analysis showed that a chief satellite with the size of SMOS would be able to pack a smaller array of this size in addition to the deputy deployment module. Fig. 5 shows the central array configuration on the chief satellite.

The chief array is tilted 30° in a cross-track direction to form a single side-looking receiver plane with the deputies on GCO. The minimal safety distance between deputy and chief of $D_{\min,C} = 10$ m is assumed for the optimization of the receiver configuration. The σ_{Gauss} parameter, given in Table IV,

TABLE IV
PARAMETER FOR ARRAY OPTIMIZATION

N Deputies	16	24	32	40	48	56
$\boldsymbol{\sigma_{Gauss}}$	40	60	80	100	120	126
N Deputies	64	72	80	88	96	
$\boldsymbol{\sigma_{Gauss}}$	144	180	200	220	240	

is set to accommodate the increasing number of satellites. Due to the nonlinearity of the optimization problem, σ_{Gauss} has to be determined empirically for each number of deputies.

The deputy satellites are each equipped with an R134a propulsion system [32] designed for close-proximity operations. The thrust magnitude and the vector error are based on the values assumed for the CanX-45 mission [23]. The relative position and velocity knowledge accuracies are assumed to be identical to the values determined for the PRISMA mission [22]. It is likely that pointing accuracies of individual CubeSats will need to be in the order of magnitude realized for the pointing accuracies of individual SMOS antennas to limit degradation of radiometric sensitivity. In this case, the pointing accuracies of the attitude control of the deputies should at least be 0.15° [15].

A. Imaging Performance

Fig. 6 shows the results of the array optimization simulations for $N = 16, 24, 32$ deputies and a minimum intersatellite distance of $D_{\min,D} = 3.5$ m. The first row of images illustrates the deputy configuration in the relative GCO plane. It can be seen that deputies are placed on a dense formation around the chief satellite. Interestingly, the optimization sets the deputies not on a ring-like formation, e.g., a Reuleaux formation [33], but in a cluster revolving around the chief satellite. This stems from the second Gaussian term in the optimization function, which favors a clustered placement of satellites, resulting in a dense, origin-centered sampling of the (u, v) plane.

The spatial frequency coverage of the aggregated array relative to boresight is depicted in the second row of Fig. 6. Each line represents the coverage of a single baseline during an overflight of a target area. The images from left to right show an increasingly homogeneous and dense sampling of the spatial frequencies due to the addition of deputies. The green lines visualize the frequency coverage of the baselines between deputies, while the blue lines visualize the baselines between the chief array and the deputy satellites. The color distinction highlights the importance of the chief array, which greatly increases the density coverage of the spatial frequency plane. The last row in Fig. 6 shows the resulting PSF at boresight, as it allows the extraction of the best-case angular resolution of the given configuration. Two effects are clearly visible. First, it can be seen that an increase in the number of deputies will lead to a tighter main lobe, i.e., a higher spatial resolution ($\Delta\xi = 1.1°$ for $N = 16$ to $\Delta\xi 0.79°$ for $N = 32$). This can be attributed to a larger diameter of the spatial frequency

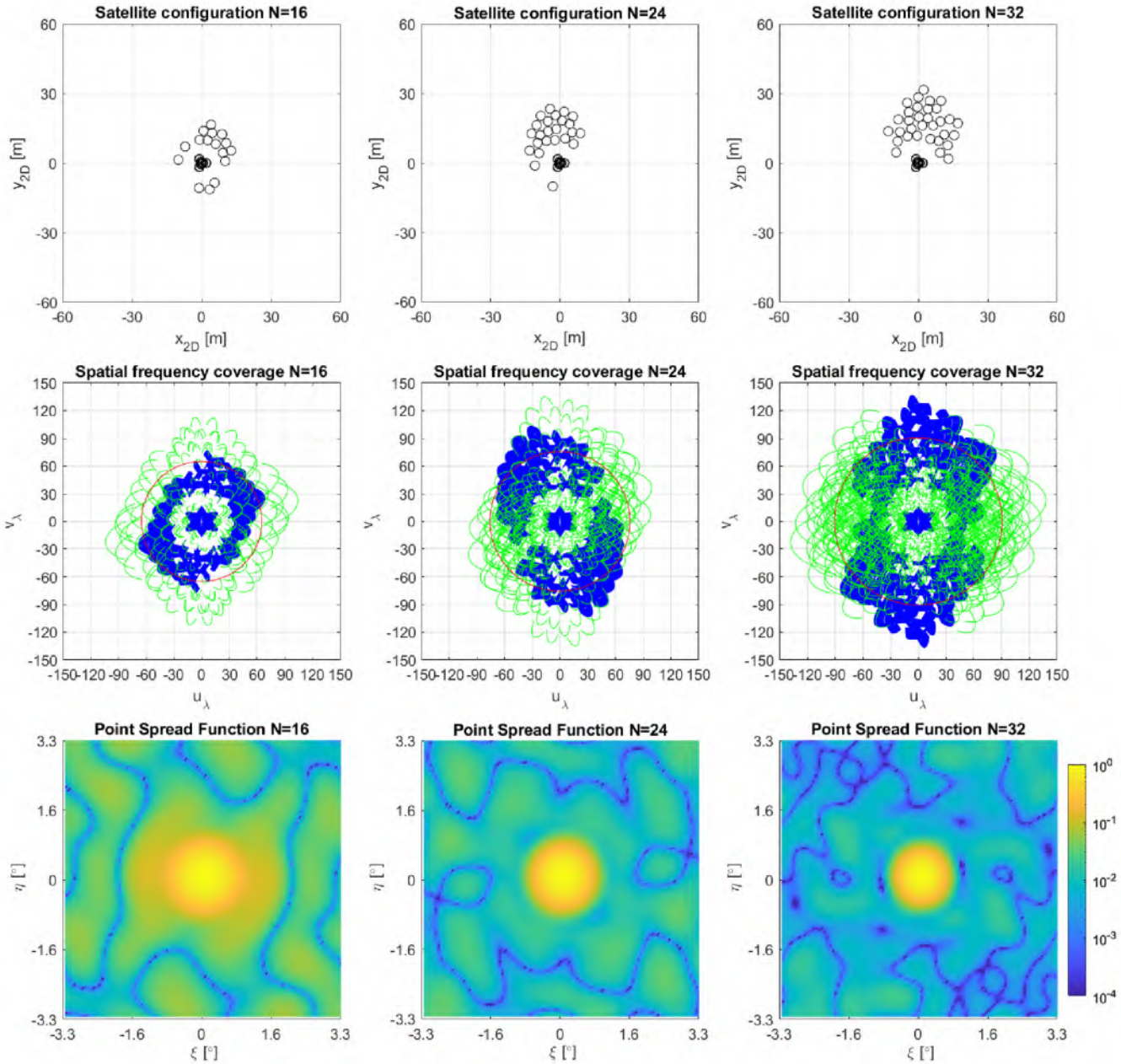

Fig. 6. Illustration of the relationship between the optimized deputy configuration (top row), sampling of the spatial frequency domain (middle row) and the PSF (bottom row) for $N = 16, 24, 32$ (columns) and a minimum intersatellite distance of 3.5 m. In the first row, the configurations are shown in the optimization coordinate system. The second row shows the visibility samples (blue: chief/deputy baselines and green: deputy/deputy baselines) in the (u, v) plane with the red circle denoting the distance $\rho_{\max}$. Finally, the last row shows contour plots of the PSF of the respective arrays.

coverage. Second, a reduction of the sidelobe levels can be observed with an increase in the number of deputies. This is attributable to the denser coverage of the spatial frequencies.

In contrast to the PSF of correlation arrays with regular antenna distances, the PSF in Fig. 6 shows no dominant sidelobes. Instead, the entire region around the main beam is more akin to an elevated plateau. A plateau outside of the main beam in the PSF leads to a response from sources outside of the focused pixel. The plateau is caused by oversampling and undersampling of regions within the spatial frequency plane. To quantify the level of the plateau, the mean sidelobe level (MSLL) is defined, denoting the mean PSF response outside of the main beam. The MSLL declines from MSLL $= -14$ dB at $N = 16$ to MSLL $= -20.2$ dB at $N = 32$.

For the observation of extended sources, a Gaussian distribution of samples [26] was shown to lead to lower sidelobes

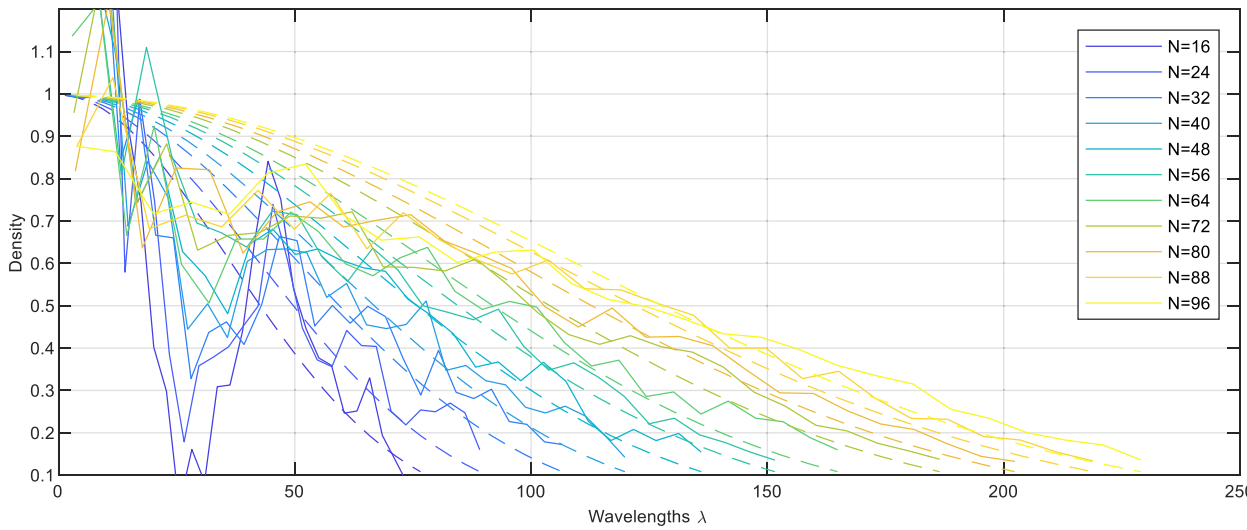

Fig. 7. Solid lines denote the actual radial distribution of spatial frequency samples for the optimized configurations. The colors denote the number of satellites used in each configuration (blue for 16 deputies to yellow for 96 deputies). The dashed lines denote a Gaussian distribution of equal standard deviations for each configuration.

TABLE V
COSINE SIMILARITY FOR VISIBILITY DISTRIBUTIONS

N	16	24	32	40	48	56	64	72	80	88	96
Value	0.79	0.85	0.88	0.92	0.95	0.97	0.97	0.98	0.98	0.99	0.99

in interferometric arrays. Thus, the degree to which the radial distribution of samples resembles a Gaussian distribution can be used as a quality measure of the optimized configuration. Fig. 7 illustrates the radial distribution of samples in the (u, v) plane for configurations of different numbers of deputies and $D_{\min,D} = 3.5$ m (solid line). In all cases, the sample distribution exhibits clear deviations from the Gaussian distribution of equal standard deviation (dashed line). This is due to the two constraints on satellite distances, i.e., the necessity to keep safety distances to avoid the collision. The safety distance to the chief satellite $D_{\min,C}$ is responsible for the large drop in sample density at approx. 30 wavelengths from the origin for configurations with few deputies. In general, the addition of deputies can be seen to lead to a better recreation of the Gaussian distribution and denser (u, v) plane coverage. The similarity between the ideal Gaussian and the actual radial distribution can be quantified with the cosine similarity [34], as displayed in Table V. A larger cosine similarity signifies a greater similarity in distribution.

The ground spatial resolution at boresight and the sensitivity of aggregated arrays for configurations with up to 96 deputies are given in Fig. 8. As a result of the increasing diameter of the array, the ground spatial resolution increases asymptotically to a minimum of 5.64 km at boresight or 4.91 km at Nadir for 96 deputies. Any further improvement of the resolution becomes costlier in terms of required deputies since an additional percentage change in diameter requires more covered area in the spatial frequency domain. The radiometric

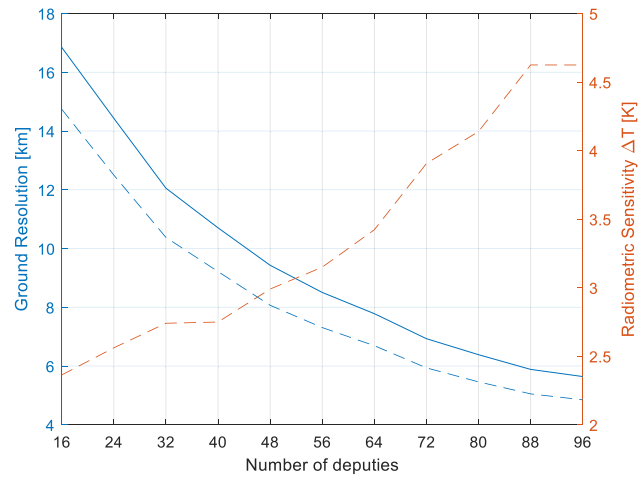

Fig. 8. Resolution in km (blue solid line) at boresight at Nadir (dashed blue line) and sensitivity in Kelvin (red dashed line) for configurations with N deputies and $D_{\min,D} = 3.5$ m.

sensitivity of the system deteriorates from 2.36 K with 16 deputies to 4.62 K at configurations with 96 deputies. The sensitivity of the system deteriorates due to an increase in synthesized antenna diameter, i.e., an improvement of angular resolution, with an increasing number of baselines present within the aggregated array (see Fig. 6). In particular, the increase in the number of baselines leads to a larger weighting term in (18), while the increase in the resolution leads to an increase of the beam filling factor $\Omega_{\text{ant}}/\Omega_{\text{pix}}$.

According to the radiometric uncertainty principle [35], the product of the angular resolution and the radiometric sensitivity should be a constant, as indicated in Table VI. The deviations of $\Delta T \cdot \theta_{ta}$ (from a constant) can be attributed to the different degrees of required density weighting. Some configurations require a stronger density weighting to compensate for an inferior optimization solution.

TABLE VI

ANGULAR RESOLUTION θ_w AND RADIOMETRIC SENSITIVITY ΔT OF SATELLITE CONFIGURATIONS

N Deputies	16	24	32	40	48	56
θ_w [°]	1.1	0.94	0.79	0.7	0.62	0.56
ΔT [K]	2.36	2.56	2.74	2.75	2.99	3.15
$\Delta T \cdot \theta_w$ [°K]	2.61	2.43	2.16	1.93	1.85	1.75
N Deputies	64	72	80	88	96	
θ_w [°]	0.51	0.45	0.42	0.38	0.37	
ΔT [K]	3.42	3.91	4.14	4.62	4.62	
$\Delta T \cdot \theta_w$ [°K]	1.74	1.77	1.73	1.79	1.71	

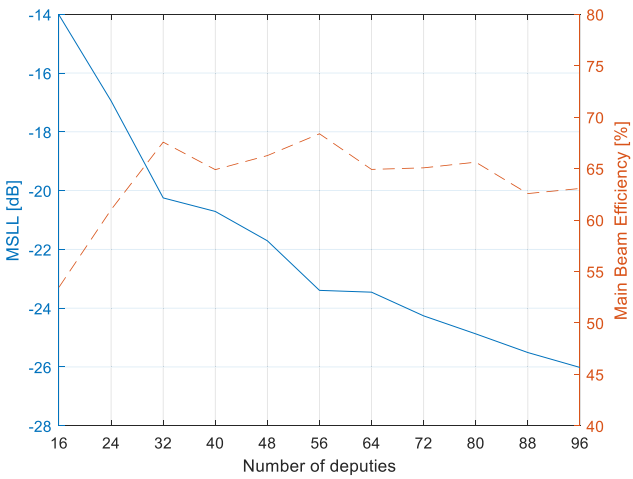

Fig. 9. MSLL in dB (solid line) and MBE in % (dashed line) for configurations with N deputies and $D_{\min,D} = 3.5$ m.

Independent of the number of satellites used, the sensitivity stays significantly below that of current systems such as SMOS (0.33 K for cold backgrounds) [36].

Fig. 9 shows the progression of the MSLL and the MBE of the aperture synthesis radiometer formed with different numbers of satellites. Especially for configurations with a higher number of deputies, the PSF shows a relatively homogenous residual response in the areas outside the main sidelobe. There are no distinct "largest" sidelobes at all. The MSLL shows a continuous decline from -14 to -26 dB for an increasing number of deputy satellites. The decline is simply due to the denser and increasingly Gaussian distribution of the spatial frequency samples in the (u, v) plane. With efficiencies up to 68%, the proposed arrays move toward efficiencies of monolithic arrays [15]. The MBE stays relatively constant across the different configurations. This is because the improvement in spatial resolution is compensated by the effect of a declining level of MSLL. While a decline of MSLL in the nonmain lobe region of the PSF increases the energy concentrated in the main beam, a tighter main beam enlarges the sidelobe region.

B. System Implications

Fig. 10 illustrates the mean 3-D rms position control accuracy of the autonomous controller for each satellite within the

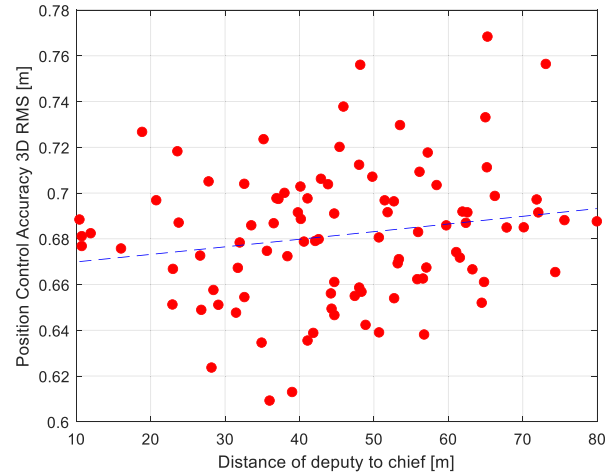

Fig. 10. Deputy position control accuracy as 3-D rms error [m] for the formation of $N = 96$ deputies and $D_{\min,D} = 3.5$ m.

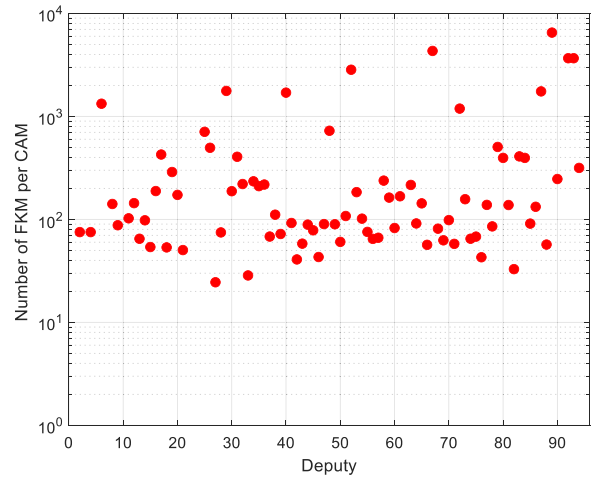

Fig. 11. Number of FKM per necessary CAM of each satellite per orbit for the formation of $N = 96$ deputies and $D_{\min,D} = 3.5$ m.

$N = 96$ configuration, ordered by distance to the chief. The position control accuracy of the deputies exhibits a Gaussian distribution around the rising mean (blue dashed line), staying within $\sigma_{3DPos} = 0.77$ m. It can be seen that the position control accuracy declines slightly with an increasing distance, which is consistent with increasing perturbations due to the Earth oblateness effect. The variations around the mean are caused by the Gaussian nature of the imposed navigation errors, i.e., the GNC position, the GNC velocity error, and the thruster errors. The exact angular position on a GCO of a given distance seems to have little impact on fuel consumption, aside from the orbiting distance to the chief.

Fig. 11 shows the number of regular FKM before an additional CAM has to be performed to avoid the violation of the minimum safety distance by any deputy. The safety distance has been assumed as the combined maximum dimension of the two cubic deputy satellites and an additional interdeputy safety margin of 0.9 m, i.e., $R_{\text{Coll}} = \sqrt{3} \cdot L_{\text{Cube}} + 0.9$, with L_{Cube} being the side length of the deputy. The median CAM frequency is given as a single CAM per 143 FKM, which would amount to 0.046 additional CAM per orbit. Individual deputies, however, require collision avoidance more frequently with up to one CAM every 24.5 FKM or 0.27 additional CAM

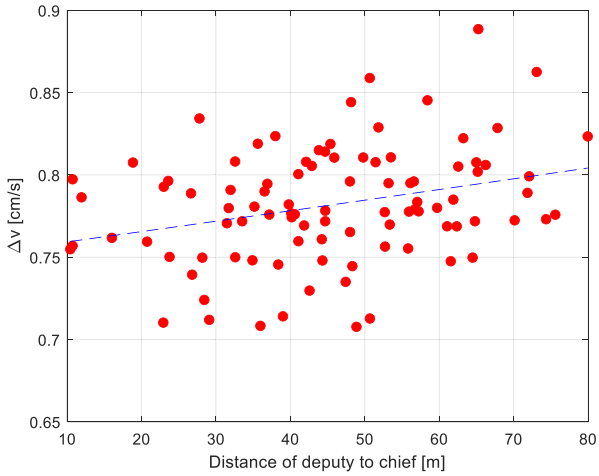

Fig. 12. Average fuel consumption Δv [cm/s] for formation maintenance per orbit for the formation of $N = 96$ deputies and $D_{\min,D} = 3.5$ m.

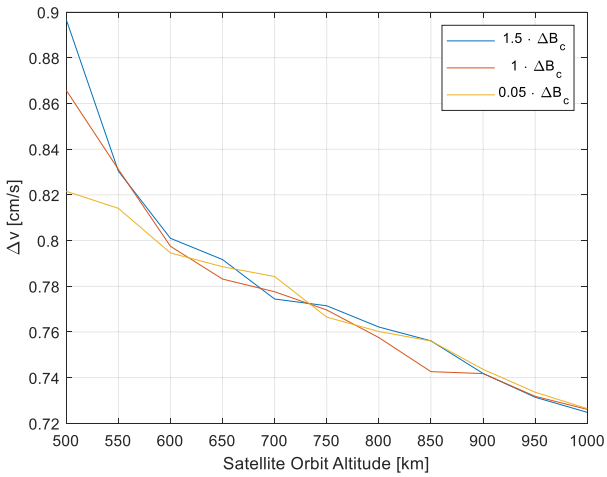

Fig. 13. Average fuel consumption Δv [cm/s] for formation maintenance per orbit and deputy for the formation of $N = 56$ deputies and $D_{\min,D} = 3.5$ m over varying orbit altitude and difference in ballistic coefficient (colors) between deputies and the chief satellite.

per orbit. A higher frequency of CAMs is required by a closer reference distance to any other satellite or a lower position control accuracy. The collision risk can be further lowered either by increasing the minimum distance of all deputies $D_{\min,D}$ or by iteratively repositioning single satellites.

While the additional CAMs will add to the fuel consumption of the system, the fuel budget will still be dominated by the standard periodic FKM. The added fuel consumption due to CAM, however, will shorten the lifetime of the system by 4.1%.

Fig. 12 shows the mean fuel consumption Δv per satellite and orbit required for the periodic FKM that are performed every control period T_{pwm}. The fuel consumption behaves analogously to the position control accuracy in Fig. 10, rising quasi-linear with increasing distance to the chief. Fuel consumption per deputy stays within 0.9 cm/s per orbit, even for the deputies on the outer rim of the aperture synthesis antenna array. Assuming that the CAM consumes similar amounts of fuel, as the FKM, a swarm lifetime of 150 days could be supported.

The impact of the orbit altitude and the difference in ballistic coefficients between deputy and chief satellites on the average fuel consumption per orbit and deputy is given in Fig. 13. The difference in ballistic coefficient is varied as a multiple of the difference assumed in Table II. The graph shows that aerodynamic drag only becomes relevant for a system orbit altitude of less than 600 km, where there is a divergence of the fuel consumption. Above these altitudes, even larger differences in ballistic coefficients do not impact the fuel budget of the system. This result confirms that the driver for the fuel consumption is in fact the inaccuracy of the deputy orbit control systems.

IX. Technical Challenges

A number of technological challenges need to be addressed before the practical implementation of a swarm-based system can take place.

A. Propulsion Systems

The lifetime of the system is calculated by assuming a standard cold-gas propulsion system with a low specific impulse of $I_{\text{sp}} = 40$ s. In order to obtain a lifetime of three years, it would be necessary to use a propulsion system capable of delivering at least $I_{\text{sp}} = 292$ s. While electrical propulsion engines are capable of delivering these specific impulses, it will be a challenge to meet the high energy demand of such systems. However, new miniaturized micropulsed plasma thruster systems [37] might exhibit the thrust to power ratio that might be compatible with the investigated swarm-based radiometer concept.

B. Position Knowledge

A swarm-based synthetic aperture radiometer will require an extremely precise knowledge of the antenna phase centers to avoid degradation of the radiometric sensitivity. For example, the rms of the antenna phase center positioning error is estimated to be around 0.6 mm at the center measurement frequency of 1.4 GHz for a 1° maximum phase error. For an SMOS-type array, Camps [14] reported that the positions of the antenna phase centers must be known to millimeter-level accuracy to ensure a reasonable radiometric accuracy for soil moisture retrieval. While this requirement cannot be directly applied to the present case, due to the different array configurations, they can provide a first reasonable estimate on the order of magnitude required.

Current GNC positioning solutions for CubeSats are not capable of delivering this accuracy. It is conceivable that a pulse-based proximity navigation system might be capable of delivering the required position knowledge. This navigation system could possibly be based on the required intersatellite communication infrastructure.

C. Synchronization

Accurately measuring the signal phases will require a synchronization accuracy in the order of magnitude of 2 ps (assuming a 1° permissible phase error) over a single measurement period of 10 ms. The short measurement period ensures that signal phases can be measured with the required

phase error of 1°. Space-qualified Oven-Controlled Crystal Oscillators (OCXOs) with Allan variances in the order of $\sigma_y = 10^{-12}$ [38] are capable of delivering the required short-term stability. These would be placed on individual satellites. A two-way microwave phase-locked loop (PLL) could keep OCXO oscillators on deputies synchronized with the master oscillator on the chief once calibrated. The practical implementation of this synchronization scheme on a CubeSat swarm has not been performed so far.

X. Conclusion and Outlook

In this study, the orbit mechanics and imaging performance were explored for the definition and development of an Earth-observing satellite-swarm-based MISAR mission scenario. A design and simulation tool was developed for such a system and demonstrated by simulating configurations with varying numbers of deputy satellites. Simulation results show that the placement of deputy satellites on GCO in optimized formations around the chief satellite enables the creation of aperture synthesis antenna arrays capable of reaching main beam efficiencies of up to 68%. It was shown that angular resolutions θ_w can reach 0.37° (5.64 km at boresight) for configurations with 96 deputies. This represents an approximate quintuple improvement over the spatial resolution reported for the SMOS instrument [3]. While radiometric sensitivities of the simulated configurations do not reach the values of previous systems, e.g., SMOS with 0.33 K, sensitivities could be sufficient to add significant value to science applications. Especially, the configurations with 56 deputies seem to represent a good tradeoff between spatial (∼9 km) and radiometric resolution (3.15 K). This could meet the requirements set for soil moisture monitoring [39].

Simulations show that state-of-the-art nanosatellite orbit control systems are capable of positioning satellites on close-proximity GCO orbits with a relative position control accuracy below 1-m rms. The attainable position control accuracy of a fully autonomous deputy satellite is shown to rise linearly with distance to the chief satellite.

Furthermore, it was shown that fuel consumption for regular FKMs on these GCO stays below 0.9 cm/s per orbit. Assuming state-of-the-art cold gas propulsion systems, the lifetime of the system could be up to 150 days. With the utilization of next-generation MEMS-based propulsion, e.g., water microresistojets [40], it is plausible that the lifetime can be extended to significantly longer durations, which will be needed for Earth observation missions including missions focused on larger period hydrologic and climatologic phenomena.

The given investigation represents an attempt to show the feasibility of a swarm-based aperture synthesis radiometer with one chief and many deputies from an orbit mechanical perspective. Further research must be conducted on other issues surrounding the implementation of such a system. These aspects include a deeper investigation of the following.

1) *In-Depth Quantitative Analysis of the Impact of Error Sources:* This study investigates an ideal system. A further in-depth study of the impact of error sources on the radiometric performance must be carried out. In particular, these refer to investigations of antenna errors (e.g., antenna position errors, antenna pattern phase and gain ripples, antenna pointing errors, errors in the antenna coupling, and the cross-polarization), channel errors, and baseline errors [15].
2) *Deputy Deployment:* Research is required on the sequence of deployment, the design of the dispenser module, and requirements for chief attitude control.
3) *Onboard Data Handling:* Processing architecture of ARU data on the chief satellite and requirements for data downlink system.
4) *Intersatellite Links:* Close-proximity, high-bandwidth communication systems need more research to enable low-power solutions for CubeSats [41].
5) *Risk Reduction for Contingency Events:* A strategy needs to be developed to ensure that defunct deputies are safely removed from the swarm without endangering any other satellites.

With further progress in DGNSS, CubeSat propulsion, satellite-swarm control, and miniaturization of spacecraft electronics, it is reasonable to believe that a swarm-based aperture synthesis radiometer could be a feasible way of improving radiometry-based Earth science data acquisition. For example, the usage of dual-channel receivers could improve the radiometric sensitivity of the system by a factor of $\sqrt{2}$.

Moreover, it is possible that this concept could be applied to other applications, such as artificial signal or radio interference detection, which usually works with much higher signal-to-noise ratios. Position knowledge accuracy requirements for these applications might be relaxed so that the accuracy in the centimeter range might be adequate.

Appendix A

The following method was used for the calculation of the discrete constant gain matrix K for the autonomous control of the deputy satellites. The discrete constant gain matrix K is given by

$$K = \left(B_d^T \bar{P} B_d + R\right)^{-1} B_d^T \bar{P} \Phi \tag{19}$$

where B_d is defined as

$$B_d = \left(\int_0^{T_{\text{pwm}}} e^{A\tau} d\tau\right) B \tag{20}$$

with

$$\Phi = e^{A \cdot T_{\text{pwm}}}. \tag{21}$$

The state-space representation of the Clohessy–Wiltshire dynamics is described by

$$A = \begin{bmatrix} 0 & 0 & 0 & 1 & 0 & 0 \\ 0 & 0 & 0 & 0 & 1 & 0 \\ 0 & 0 & 0 & 0 & 0 & 1 \\ 3n^2 & 0 & 0 & 0 & 2n & 0 \\ 0 & 0 & 0 & -2n & 0 & 0 \\ 0 & 0 & -n^2 & 0 & 0 & 0 \end{bmatrix}. \tag{22}$$

The matrix B is described by

$$B = \begin{bmatrix} 0_{3\times 3} \\ I_{3\times 3} \end{bmatrix}. \tag{23}$$

The matrix $\bar{P}$ in (19) can be determined by numerically solving the DARE equation given by

$$\Phi^T \bar{P} \Phi - \bar{P} - \Phi^T \bar{P} B_d \left(B_d^T \bar{P} B_d + R \right)^{-1} B_d^T \bar{P} \Phi + Q = 0. \quad (24)$$

The weighting matrices used for the calculation of the control matrices for the autonomous orbital control of the deputy satellites are

$$R = \frac{1.4}{n^2} \begin{bmatrix} 1 & 0 & 0 \\ 0 & 1 & 0 \\ 0 & 0 & 1 \end{bmatrix} \quad (25)$$

$$Q = \begin{bmatrix} 1.1n^2 & 0 & 0 & 0 & 0 & 0 \\ 0 & 1.1n^2 & 0 & 0 & 0 & 0 \\ 0 & 0 & 1.1n^2 & 0 & 0 & 0 \\ 0 & 0 & 0 & 0.78 & 0 & 0 \\ 0 & 0 & 0 & 0 & 0.78 & 0 \\ 0 & 0 & 0 & 0 & 0 & 0.78 \end{bmatrix}. \quad (26)$$

A more elaborate description of the optimization of control matrices via the DARE and the state-space matrices can be found in [23].

Appendix B

The radiometric sensitivity in (18) was determined using the general derivation given by Wrobel *et al.* [30] for a synthesis image of a radio interferometer. This derivation was chosen as it considers the density weighting technique applied within this study. The estimated brightness temperature $\hat{T}(x_0, y_o)$ given in (1) may also be stated as the weighted sum of the individual baseline measurements

$$\hat{T}(x_0, y_o) = \frac{\sum_j \bar{W}_j \cdot \hat{T}_j(x_0, y_0)}{\sum_j \bar{W}_j}. \quad (27)$$

To calculate the system radiometric sensitivity, only the point at the origin $x_0 = 0$ and $y_0 = 0$ is considered since it represents the best-case radiometric sensitivity. The associated variance $\Delta\hat{T}^2(0, 0)$ in brightness temperature is the sum of the squared variances of each temperature measurement $\Delta\hat{T}_j(0, 0)$ of baseline j over all timesteps. The square root of $\Delta\hat{T}^2(0, 0)$ is then

$$\Delta\hat{T}(0, 0) = \frac{1}{\sum_j \bar{W}_j} \sqrt{\sum_j \bar{W}_j^2 \cdot \Delta\hat{T}_j{}^2(0, 0)}. \quad (28)$$

Assuming equal sensitivity of each ARU, one can assume equal $\Delta\hat{T}_j$ for all baselines. The fluctuation of brightness temperature for each baseline can be given as a function of the estimated flux density fluctuations $\Delta\hat{S}_j$ using the Rayleigh–Jeans relation

$$\Delta\hat{T}_j = \frac{\lambda^2}{2k} \cdot \frac{1}{\Omega_{\text{Pix}}} \cdot \Delta\hat{S}_j. \quad (29)$$

According to Wrobel and Walker [30], the flux density fluctuations $\Delta\hat{S}_j$ for a single sideband receiver and a Gaussian predetection filter can be given as

$$\Delta\hat{S}_j = \frac{2k}{A_{\text{eff}}} \cdot \frac{T_{\text{sys}}}{\sqrt{B\tau_{\text{eff}}}} \cdot \frac{1}{\sqrt[4]{2}}. \quad (30)$$

Combining (26)–(28) with $\Omega_{\text{ant}} = \lambda^2 / A_{\text{eff}}$ yields the radiometric sensitivity for the system at boresight

$$\Delta T(0, 0) = \frac{\Omega_{\text{ant}}}{\Omega_{\text{pix}}} \cdot \frac{T_{\text{sys}}}{\sqrt[4]{2} \cdot \sqrt{B\tau_{\text{eff}}}} \frac{\sqrt{\sum_j \bar{W}_j^2}}{\sum_j \bar{W}_j}. \quad (31)$$

Acknowledgment

The authors would like to thank Ralph Kahle, Michael Kirschner, Jan Eilers, Thomas Neff, and Alberto Moreira for crucial support in the preparation of this article.

References

[1] D. Entekhabi *et al.*, "The soil moisture active passive (SMAP) mission," *Proc. IEEE*, vol. 98, no. 5, pp. 704–716, May 2010.

[2] J. P. Wigneron, A. Chanzy, and P. Waldteufel, *Retrieval Capabilities of LB and 2-D Interferometric Radiometry Over Land Surfaces (SMOS Mission)*. Amsterdam, The Netherlands: VSP, Jan. 2000.

[3] *SMOS Data Products Brochure*, European Space Agency, Paris, France, Nov. 2017.

[4] *SMAP Handbook Soil Moisture Active Passive*, Jet Propulsion Laboratory, NASA, Washington, DC, USA, Jul. 2014.

[5] L. Kilic *et al.*, "Expected performances of the Copernicus imaging microwave radiometer (CIMR) for an all-weather and high spatial resolution estimation of ocean and sea ice parameters," *J. Geophys. Res., Oceans*, vol. 123, no. 10, pp. 7564–7580, Oct. 2018.

[6] S. Mecklenburg, "ESA's Soil Moisture and Ocean Salinity mission: From science to operational applications users," *Remote Sens. Environ.*, vol. 180, pp. 3–18, Jul. 2016.

[7] J. P. Walker and P. R. Houser, "Requirements of a global near-surface soil moisture satellite mission: Accuracy, repeat time, and spatial resolution," *Adv. Water Resour.*, vol. 27, no. 8, pp. 785–801, Aug. 2004.

[8] S. Voigt, "Global trends in satellite-based emergency mapping," *Science*, vol. 353, no. 6296, pp. 247–252, Jul. 2016.

[9] A. Ajmar, "Response to flood events: The role of satellite-based emergency mapping and the experience of the Copernicus emergency management service," *Flood Damage Surv. Assess. Insights Res. Pract.*, vol. 228, pp. 213–228, Jun. 2017.

[10] A. K. S. El Maghraby, A. Kiyoshic, A. Grubišić, C. Colombo, and A. Tatnall, "A novel interferometric microwave radiometer concept using satellite formation flight for geostationary atmospheric sounding," *IEEE Trans. Geosci. Remote Sens.*, vol. 56, no. 6, pp. 3487–3498, Jun. 2018.

[11] F. Y. Hadaegh, S.-J. Chung, and H. M. Manohara, "On development of 100-Gram-class spacecraft for swarm applications," *IEEE Syst. J.*, vol. 10, no. 2, pp. 673–684, Jun. 2016.

[12] S.-H. Mok, J. Guo, E. Gill, and R. T. Rajan, "Lunar orbit design of a satellite swarm for radio astronomy," in *Proc. IEEE Aerosp. Conf.*, Mar. 2020, pp. 1–9.

[13] B. S. Schwarz, A. R. L. Tatnall, and H. G. Lewis, "Coastal salinity measurement using a Doppler radiometer," *Adv. Space Res.*, vol. 50, no. 8, pp. 1138–1149, Oct. 2012.

[14] A. Camps, "Application of interferometric radiometry to Earth observation," Ph.D. dissertation, Dept. Signal Theory Commun., Caltech Submillimeter Observatory, Univ. Politècnica de Catalunya, Barcelona, Spain, 1996.

[15] A. Camps and C. Swift, "Observation, a two-dimensional Doppler-radiometer for Earth," *IEEE Trans. Geosci. Remote Sens.*, vol. 39, no. 7, pp. 1566–1572, Jul. 2001.

[16] A. Camps *et al.*, "Microwave imaging radiometers by aperture synthesis—Performance simulator (Part 1): Radiative transfer module," *J. Imag.*, vol. 2, no. 2, p. 17, May 2016.

[17] H. Park and Y. H. Kim, "Improvement of a Doppler-radiometer using a sparse array," *IEEE Geosci. Remote Sens. Lett.*, vol. 6, no. 2, pp. 229–233, Apr. 2009.

[18] R. A. Thompson, J. Moran, and G. Swenson, *Interferometry and Synthesis in Radio Astronomy*. Cham, Switzerland: Springer, 2017.

[19] K. Alfriend, *Spacecraft Formation Flying*. Amsterdam, The Netherlands: Elsevier, 2010.

[20] G. Xu and D. Wang, "Nonlinear dynamic equations of satellite relative motion around an oblate Earth," *J. Guid., Control, Dyn.*, vol. 31, no. 5, pp. 1521–1524, Sep. 2008.

[21] D. Morgan and S.-J. Chung, "Swarm-keeping strategies for spacecraft under J2 and atmospheric drag perturbation," *J. Guid. Control Dyn.*, vol. 35, no. 5, Aug. 2012.
[22] M. D'Errico, *Distributed Space Missions for Earth System Monitoring*. Cham, Switzerland: Springer, 2013, p. 623.
[23] J. Eyer, "A dynamics and control algorithm for low Earth orbit precision formation flying satellites," Ph.D. dissertation, Inst. Aerosp. Stud., Toronto, Univ. Toronto, Toronto, ON, USA, 2009.
[24] R. P. Patera, "General method for calculating satellite collision probability," *J. Guid., Control, Dyn.*, vol. 24, no. 4, pp. 716–722, 2001.
[25] F. Boone, "Interferometric array design: Optimizing the loctions of the antenna pads," *Astron. Astrophys.*, vol. 377, no. 1, pp. 268–376, Oct. 2001.
[26] D. Woody, "Radio interferometer array point spread functions, I. Theory and statistics," *ALMA MEMO*, vol. 389, pp. 1–8, Aug. 2001.
[27] Y. Su, "Optimization of interferometric array configurations by 'sieving' u–v points," *Astronomy Astrophys.*, vol. 414, no. 1, pp. 389–397, Jan. 2004.
[28] A. Conn, N. Gould, and P. Toint, "A globally convergent Lagrangian barrier algorithm for optimization with general inequality constraints and simple bounds," *Math. Comput. Amer. Math. Soc.*, vol. 66, no. 217, pp. 261–288, 1997.
[29] D. Briggs, "High fidelity deconvolution of moderately resolved sources," Ph.D. dissertation, New Mexico Inst. Mining Technol., Socorro, NM, USA, Mar. 1995.
[30] J. Wrobel and R. Walker, "Sensitivity," in *Proc. Synth. Imag. Radio Astron. 11 ASP Conf. Ser.*, vol. 180, 1999, pp. 171–186.
[31] J. B. Hagen and D. T. Farley, "Digital-correlation techniques in radio science," *Radio Sci.*, vol. 8, nos. 8–9, pp. 775–784, Aug./Sep. 1973.
[32] V. Industries. (2020). *Reaction Control Propulsion Module*. Accessed: Jul. 20, 2020. [Online]. Available: https://www.vacco.com/space/chems-overview
[33] N. Jin and Y. Rahmat-Samii, "Analysis and particle swarm optimization of correlator antenna arrays for radio astronomy applications," *IEEE Trans. Antennas Propag.*, vol. 56, no. 5, pp. 1269–1279, May 2008.
[34] L. Lee, "Measures of distributional similarity," in *Proc. 37th Annu. Meeting Assoc. Comput. Linguistics Comput. Linguistics*, 1999, pp. 1–8.
[35] H. Park, A. Camps, M. G. Choi, and Y.-H. Kim, "Radiometric resolution of motion-induced synthetic aperture radiometer," *IEEE Geosci. Remote Sens. Lett.*, vol. 8, no. 4, pp. 715–719, Jul. 2011.
[36] European Space Agency. *SMOS (Soil Moisture and Ocean Salinity) Mission*. eoPortal Directory. Accessed: Jul. 20, 2020. [Online]. Available: https://directory.eoportal.org/web/eoportal/satellite-missions/s/smos
[37] S. Miller, M. Walker, J. Agolli, and J. Dankanich, "Survey and performance evaluation of small-satellite propulsion technologies," *J. Spacecraft Rockets*, vol. 58, no. 1, pp. 220–230, 2021.
[38] M. Weiss, "Synchronisation of bistatic radar systems," in *Proc. IEEE Int. Int. IEEE Int. Geosci. Remote Sens. Symp. (IGARSS)*, Sep. 2004, pp. 1750–1753.
[39] *SMOS-Next: USERs' Group Meeting*, CESBIO, Toulouse, France, 2014.
[40] A. Cervone, B. Zandbergen, D. C. Guerrieri, M. D. A. C. E. Silva, I. Krusharev, and H. van Zeijl, "Green micro-resistojet research at Delft University of technology: New options for cubesat propulsion," *CEAS Space J.*, vol. 9, no. 1, pp. 111–125, Mar. 2017.
[41] NASA. (May 4, 2020). *State of the Art of Small Spacecraft Technology Communications*. NASA. Accessed: Jul. 11, 2020. [Online]. Available: https://www.nasa.gov/smallsat-institute/sst-soa/communications

Mark Lützner received the Diploma degree in aerospace engineering from the University of Stuttgart, Stuttgart, Germany, in 2013. He is currently pursuing the Ph.D. degree with the Universität der Bundeswehr, Munich, Germany.

From 2013 to 2014, he was a Verification Engineer for the Small Satellite Programme with the University of Stuttgart, before completing the Young Graduate Trainee (YGT) Programme of the European Space Agency (ESA) in 2015. From 2016 to 2017, he was a Management Consultant for the boutique consultancy SpaceTec Partners, Munich. Since 2017, he has been with the Microwaves and Radar Institute (HR), German Aerospace Center (DLR), Weßling, Germany. He is currently an Assessor for the Ministry of Business, Innovation and Employment (MBIE) of New Zealand. He has been a Guest Lecturer with the Munich University of Applied Sciences, Munich. His main research interests include nanosatellite swarms, satellite formation flight, and microwave applications for satellite formations.

Thomas Jagdhuber (Senior Member, IEEE) received the Diploma degree in physical geography, physics, remote sensing, and geoinformatics from Ludwig Maximilian University of Munich (LMU), Munich, Germany, and the Technical University (TUM) of Munich, Munich, in 2006, and the Ph.D. degree in hydrology from the Faculty of Science, University of Potsdam, Potsdam, Germany, in 2012.

Since 2007, he has been with the Microwaves and Radar Institute (HR), German Aerospace Center (DLR), Weßling, Germany. From 2014 to 2019, he was a Yearly Visiting Scientist with the Massachusetts Institute of Technology (MIT), Boston, MA, USA, contributing to the preparation and continuation of the Soil Moisture Active Passive (SMAP) and SMAP/Sentinel-1 missions. He is also a Lecturer with the University of Jena, Jena, Germany, and the University of Augsburg, Augsburg, Germany. His main research interest includes physics-based multisensor data integration with a focus on active and passive microwave interaction theory and polarimetric techniques for hydrological, agricultural, ecological, and cryospheric parameter modeling and estimation.

Dr. Jagdhuber was honored with the DLR Science Award for his research on polarimetric SAR decomposition techniques in 2014. Together with Prof. Entekhabi (MIT), he was awarded the MIT-MISTI Grant for global water cycle and environmental monitoring using active and passive satellite-based microwave instruments. He also serves as a reviewer for several international journals and conference boards.

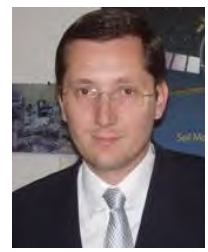

Adriano Camps (Fellow, IEEE) was born in Barcelona, Spain, in 1969. He received the Diploma degree in telecommunications engineering and the Ph.D. degree in telecommunications engineering from the Universitat Politècnica de Catalunya (UPC), Barcelona, in 1992 and 1996, respectively.

From 1991 to 1992, he was with the ENS des Télécommunications de Bretagne, Bretagne, France, with an Erasmus Fellowship. Since 1993, he has been with the Electromagnetics and Photonics Engineering Group, Department of Signal Theory and Communications, UPC, where he was an Assistant Professor and an Associate Professor in 1997 and has been a Full Professor since 2007. In 1999, he was on sabbatical leave at the Microwave Remote Sensing Laboratory, University of Massachusetts Amherst, Amherst, MA, USA. Since 1993, he has been deeply involved in the European Space Agency SMOS Earth Explorer Mission from the instrument and algorithmic points of view, performing field experiments. Since 2001, he has been studying the use of global navigation satellite system reflectometry (GNSS-R) techniques to perform the sea state correction needed to retrieve salinity from L-band radiometric observations. He has published over 216 papers in peer-reviewed journals, six book chapters, one book, and more than 450 international conference presentations. He holds 12 patents. He has advised 23 Ph.D. thesis students (more than eight ongoing) and more than 140 final projects and M.Eng. theses. According to Publish or Perish (Google Scholar), his publications have received more than 7161/10 706 citations. His H-index is 39/51 according to Scopus/Google Scholar. His research interests are focused on microwave remote sensing with a special emphasis on microwave radiometry by aperture synthesis techniques, remote sensing using signals of opportunity (GNSS-R), radio frequency detection and mitigation techniques for microwave radiometry and GNSS, and CubeSats as platforms to test novel remote sensing concepts.

Dr. Camps received several awards, including the EURopean Young Investigator (EURYI) Award in 2004, the Duran Farell Awards for Technology Transfer in 2000 and 2010, and the ICREA Acadèmia Research Awards in 2008 and 2014. He was the Copernicus Masters ESA Sentinel Small Satellite Challenge 2017 Winner and the Copernicus Masters Overall Winner for the FSSCAT mission, the first contributing mission to Copernicus based on CubeSats. He was the Technical Program Committee Chair of the International Geoscience and Remote Sensing Symposium (IGARSS) 2017 and the General Co-Chair of IGARSS 2020. He was the IEEE GRSS President from 2017 to 2018. He has been involved in the organization of several other conferences.

Hyuk Park (Senior Member, IEEE) was born in South Korea. He received the B.S. degree in mechanical engineering from the Korea Advanced Institute of Science and Technology (KAIST), Daejeon, South Korea, in 2001, and the M.S. and Ph.D. degrees in information and mechatronics from the Gwangju Institute of Science and Technology (GIST), Gwangju, South Korea, in 2003 and 2009, respectively.

In 2009, he joined the Remote Sensing Group, Polytechnic University of Catalonia (UPC), Barcelona, Spain, as a Post-Doctoral Researcher. In 2011, he was a grant holder of the National Research Foundation funded by the Korean Government. Since 2012, he has been a Research Associate with a Juan de la Cierva grant funded by the Spanish Ministry of Economy and Competitiveness. He is currently a Ramon y Cajal Fellow/Tenure-track Assistant Professor with the School of Telecommunications and Aerospace Engineering at Castelldefels (EETAC-UPC). He is also working with the Passive Remote Sensing Group, UPC, for satellite remote sensing for microwave radiometry and global navigation satellite system reflectometry. His main research interest is in the area of remote sensing, particularly passive microwave remote sensing, including system design, modeling and simulation, image processing, and small satellite applications.

Markus Peichl (Member, IEEE) was born in Sulzfeld, Germany, in 1963. He received the Diploma and Ph.D. degrees in electrical engineering from the University of Karlsruhe [now Karlsruhe Institute of Technology (KIT)], Karlsruhe, Germany, in 1990 and 1994, respectively.

Since 1990, he has been a Scientist with the Microwaves and Radar Institute, German Aerospace Center (DLR), Weßling, Germany. Since 1998, he has been leading the Microwave Sensors Group, Department for Reconnaissance and Security. He is a coauthor of one book, and the author and a coauthor of more than 300 publications. His research interests cover the development and construction of innovative and advanced radiometer and radar systems for experimental and operational purposes with respect to future spaceborne, airborne, or ground-based remote sensing projects, research on advanced image reconstruction methods, investigations on microwave sensors for applications in security and safety, and dual-use applications in agriculture and the monitoring of infrastructures. He holds three patents; the fourth one is pending.

Dr. Peichl is also a member of VDE (German Association of Electrical Engineers). From 2000 to 2010, he was a member of the Science Advisory Group of the SMOS project for European Space Agency (ESA). Since 2013, he has been a member of the Technical Committee on THz Technologies of VDI (German Association of Engineers). He has been participating on various international research groups for NATO Science and Technology Organization (STO).

Roger Förstner received the Diploma degree in aerospace engineering from the University of Stuttgart, Stuttgart, Germany, in 1998.

From 2002 to 2009, he was a Systems Engineer with Astrium GmbH (now Airbus DS), Friedrichshafen, Germany, mainly working for Europe's Mercury mission BepiColombo. Since 2009, he has been a Full Professor of space technology with the Universität der Bundeswehr, Neubiberg, Germany. He is currently the Dean of the Faculty of Aerospace Engineering and the Spokesman for the Research Center SPACE.

Matthias Jirousek was born in Gernsbach, Germany, in 1975. He received the Diploma and Ph.D. degrees in electrical engineering from the University of Karlsruhe [now Karlsruhe Institute of Technology (KIT)], Karlsruhe, Germany, in 2002 and 2012, respectively.

Since 2003, he has been with the Microwaves and Radar Institute (HR), German Aerospace Center (DLR), Weßling, Germany. He is also the chief engineer for the development of precise and flexible active calibration targets for future satellite SAR calibration missions with a focus on absolute radiometric calibration. He also serves as a Lecturer in space-borne microwave radiometry with KIT. He was responsible for research on a passive microwave imaging experimental spectrometer system based on aperture synthesis. His research concentrates on highly digitized wideband radar instruments for imaging of satellites in space and remote sensing on high altitude platforms. His main research interests are in the development and construction of highly innovative microwave sensor systems and calibration standards.